Characterization and Evolution of Organized Shallow Convection in the Trades

Hauke Schulz[1], **Ryan Eastman**[2], **Bjorn Stevens**[1]

[1]Max Planck Institute for Meteorology

[2]University of Washington

Key Points:

- Meso-scale patterns of shallow convection in the trades have distinct cloud- and environmental characteristics
- Environments are shaped by disturbances from air-masses outside the trades

Corresponding author: Hauke Schulz, `hauke.schulz@mpimet.mpg.de`

Abstract

Four previously identified patterns of meso-scale cloud organization in the trades – called *Sugar*, *Gravel*, *Flowers* and *Fish*– are studied using long-term records of ground-based measurements, satellite observations and reanalyses. A neural network trained to detect these patterns is applied to satellite imagery to identify periods during which a particular pattern is over the Barbados Cloud Observatory. Surface based remote sensing at the observatory is composited and shows that the patterns can be distinguished by differences in cloud macro-physical structures. Variations in total cloudiness among the patterns are dominated by variations in cloud-top cloudiness. Cloud amount near cloud base varies little. Each pattern is associated with a distinct atmospheric environment whose characteristics are traced back to origins that are not solely within the trades. *Sugar* air-masses are characterized by weak winds and of tropical origin. *Fish* are driven by convergence lines originating from synoptical disturbances. *Gravel* and *Flowers* are most native to the trades, but distinguish themselves with slightly stronger winds and stronger subsidence in the first case and greater stability in the latter. These results suggest that due to the tight bound of the patterns to wind and air-mass origin, the patterns with the higher cloud fraction, *Flowers* and *Fish*, will be disfavoured in a warming climate with more equable sea-surface temperatures and fewer mid-latitudinal disturbances.

1 Introduction

The organization of deep convection has long been recognized to influence the distribution of moisture and as a consequence the climate. Shallow convection, as is common in the trades for instance, is usually not thought of being organized. Rather, in the mind's eye of many researchers, trade-wind clouds were randomly distributed have little vertical development and their role in the climate system was, at best, taken for granted in early studies. Over the past twenty years however, the out-sized role of maritime shallow convection on Earth's radiation budget and discrepancies in how models predict their changes with warming (Bony & Dufresne, 2005), have made a determination of processes controlling their coverage a central focus of climate science. During this period, observational studies such as RICO (Rauber et al., 2007) and the emergence of satellite imagery with spatial resolution on the hecta-meter scale began emphasizing how shallow clouds in the trades adopt different forms of organization, often in association with precipitation development and the formation of cold pools (Zuidema et al., 2012; Seifert &

Heus, 2013; Seifert et al., 2015). More recently, studies have shown that shallow convection can be categorized into several (four) large scale patterns (Stevens et al., 2020) and the form of organization influences the net cloud radiative effects and thus may influence Earth's climate sensitivity (Bony et al., 2020).

As reviewed by Nuijens, Louise and Jakob, Christian (2020), the classification of clouds into types and patterns has a long tradition. Categorization and classification help to break a complex problem down, into more manageable pieces, and thereby help to navigate natures' complexity in ways that open it to our understanding and perception. In contrast to classifications based on particular cloud types, as defined in the *International Cloud Atlas* (WMO, 2017), or to classifications based on mean properties, recent work has emphasized the large-scale patterns defined by the tiling of mesoscale elements as a basis for categorizing trade-wind cloud regimes (Stevens et al., 2020), similar to what has been done in the past to characterize cloud fields forming in association with cold-air outbreaks, or over land, or in regions where stratocumulus clouds predominate (Agee, 1987; Atkinson B. W. & Wu Zhang J., 1996; Young et al., 2002).

Following this tradition, Stevens et al. (2020) identified four patterns – which they called *Sugar*, *Gravel*, *Flowers* and *Fish*– based purely on visual satellite imagery in the vicinity of the Barbados Cloud Observatory. Of these only *Sugar* fit the prevailing view of the trades being covered by random dustings of cumulus humilis atop the background of a dark ocean. A follow-up study by Rasp et al. (2020) showed that these four patterns can be identified not only in the region of the North-Atlantic trades studied by Stevens et al. (2020), but they form in trade-wind regimes in every ocean basin. As mentioned above, the four patterns also differ in their net cloud radiative effects. This raises the question as to whether in a warmer climate, changes in cloudiness might be manifested by a different balance in their form of organization (Bony et al., 2020).

Motivated by the potential impact on climate sensitivity and the striking differences in the visual appearance of the four patterns identified by Stevens et al. (2020), we are interested in better understanding the basic features of these four patterns, and the factors that influence their emergence. More specifically, we aim to answer the questions:

1. How do the four patterns differ in terms of the observed cloud macro-physical properties?

2. Are the different patterns associated with different large-scale environments.
3. To what extent are these large-scale differences reflective of different air mass origins?

To answer these questions we collocate the four cloud patterns of meso-scale organization as automatically detected in satellite measurements with observations made at the Barbados Cloud Observatory. This contextualization of the high-resolution ground-based cloud measurements within the meso-scale patterning enables us to get deeper insights about their characteristics in ways that are not possible using satellite measurements alone.

The methods adopted and the data used are described in Section 2. A characterization of the cloud patterns with a focus on the macro-physical properties and how it fits with our preconceptions as derived from the satellite images is given in Section 3. Further, we analyse in Section 4 the meteorological conditions under which the patterns occur and the extent to which they can be distinguished. Finally, we address the question about the evolution of the air masses giving rise to the patterns by using back-trajectories, analyzing the seasonal distribution and synoptic (large-scale weather patterns) influences in Section 5. We conclude with Section 6.

2 Method

2.1 Pattern detection of shallow convection

A crucial part of this study is the detection of the four patterns of shallow convection. We base our approach on the neural network architecture described in Rasp et al. (2020), which has been trained with 10 000 manually labeled satellite images. While these manual classifications were performed for 10 years of visible imagery captured by the Moderate Resolution Imaging Spectroradiometer (MODIS) instruments aboard the satellites AQUA and TERRA, the neural network used in this study is trained with the infrared counterpart. Use of the infrared imagery was adopted to capture the patterns on a sub-daily time-scale as they do not necessarily preserve their organization throughout the day. Using infrared data lets us apply the neural network on the infrared images captured at night, but also at much higher frequency using measurements from the geostationary satellite GOES16. While the GOES16 Advanced Baseline imager can capture images every minute for pre-selected regions, here we use only the brightness temper-

atures in the clean infrared long-wave window (channel 13; 10.46 µm) at a temporal resolution of 30 minutes.

The training of the neural network in the infrared is straight forward. Instead of using the visible images during training, the infrared imagery has been used while keeping the manual classifications the same as if the classifications were made on the infrared imagery. The mean pixel agreement between the infrared and visible neural network classifications for AQUA daylight overpasses on the north Atlantic domain used in Rasp et al. (2020) is 0.4, 0.5, 0.5, 0.2 for *Sugar*, *Gravel*, *Flowers*, and *Fish*, respectively. The to some degree lower agreement in case of *Fish* can mostly be attributed to the cloud-top height information that the infrared neural network uses to reduce false classifications of cirrus clouds that occasionally can be a carbon copy of *Fish*.

To attribute one of the four patterns to the observations made at the Barbados Cloud Observatory, each classification of the neural network is evaluated at the location of the observatory. Because the site can be at the edge of a classification and we wish to include only clear and long-lasting patterns, a 6 h time period is associated with a specific pattern if for at least half of the time (3 h) a specific pattern prevails. The three winter seasons (November through March) 2018-2020 during which GOES16 data, with its higher-resolution infrared imager, are available are used for our analysis. Because the patterns occur not equally likely, the number of detected cases differs as indicated in Tab. 1, with 42 % of the 6 h windows being associated with one of the four patterns. The remaining periods were grouped together as *Others*.

Table 1. Number of time windows that contain robustly identified patterns in the winters of 2018 (JFM), 2019 (NDJFM) and 2020 (NDJFM)

pattern	# of 6h windows	% of total
Sugar	125	9
Gravel	282	19
Flowers	77	5
Fish	138	9
Others	846	58

For the detection of the seasonal cycle of the patterns and the trajectory analysis we use a different approach. First, because the GOES16 Advanced Baseline Imager does not cover the complete North Atlantic, we base this part of the analysis on the patterns detected in images captured by MODIS during daytime AQUA overpasses. Second, because this analysis is based on MODIS the longer time-record of AQUA can be used to improve the sampling. For this purpose we use the 10 year period between 2010 and 2020 inclusive.

2.2 Back-trajectories

To analyze the origin of the patterns and the evolution of the air mass in which they are found, we calculate back-trajectories following the framework of Eastman and Wood (2016). Vertical winds are assumed to be negligible compared to the horizontal components, such that the trajectories are followed near the top of the sub-cloud (boundary) layer and kept constant at the initial height of 925 hPa. These boundary-layer trajectories are calculated using winds from the 5th European Center Reanalysis of meteorological observations (ERA5) (Hersbach et al., 2020) on a 6-hourly time step.

The back-trajectories are initialized at the center of each classification within the domain 10°N-24°N and 61°W-40°W and most closely to the AQUA overpass time. The analysis covers the winter months (November through March) of 2010-2020. Trajectories are calculated for an 84 h period and atmospheric properties along the trajectory are extracted at each 12-hour time-step coinciding with a MODIS Aqua overpass. Reanalysis variables are taken from a 1x1 degree latitude-longitude grid, with averages produced for all boxes with centers that fall within 100 km of trajectory sampling points.

2.3 Surface observations

Surface observations in the trades, where these meso-scale patterns occur, are sparse, especially those beyond standard meteorological reports from ships and buoys. The Barbados Cloud Observatory (BCO) is one exception and studies have shown that the atmosphere it samples at the most windward tip of Barbados is representative for the maritime conditions in the downwind trades more generally (Stevens et al., 2016; Medeiros & Nuijens, 2016).

The BCO uses advanced remote sensing instrumentation to measure the undisturbed marine subtropical atmosphere (Stevens et al., 2016). In this study, we use simultaneous measurements from the CORAL Ka-band cloud radar and Raman lidar to characterize clouds and their thermodynamic environment, especially the surrounding humidity structure of the clouds. These advanced remote-sensing measurements are complemented by soundings of the nearby Grantley-Adams airport to improve the statistics above clouds, which can quickly attenuate the lidar signal and make a retrieval inside and above clouds impossible. Radiosondes are launched once or twice a day, usually an hour or so of their 0 UTC and 12 UTC report times.

To detect only hydro-meteors with the cloud radar and no sea-salt aerosols, we apply a threshold of −50 dBZ as used in Klingebiel et al. (2019).

In addition to the standard surface meteorological measurements from a Vaisala WXT-520, we use the rain rate measurements from a micro-rain radar (MRR). Due to its larger sampling area compared to the also available acoustic rain sensor, it detects more reliable light and/or short rain events. However, this comes at the cost of measuring the rain rate above the surface (325 m) rather than at the surface – which likely overestimates rain amount, particularly for light rain.

2.4 Cloud entity classification

The identifications of meso-scale patterns of shallow convection are supplemented with cloud-type classifications derived from the BCO measurements.

Macro-physical properties of clouds down to single cloud entities are retrieved based on the segmentation of the radar reflectivity. Individual clouds are identified by testing the connectivity of radar retrievals in height and time. Since a main part of this study focuses on stratiform layers, we use a running window of 100 s in time and only direct connections in the vertical to account for the fact, that the stratiform layers can be so thin that they are not continuously detected by the radar. To exclude false classifications as much as possible due to slanted cumulus clouds that can be falsely detected as stratiform clouds, we consider only clouds with a pass time of 2 min or more for the cloud entity analysis.

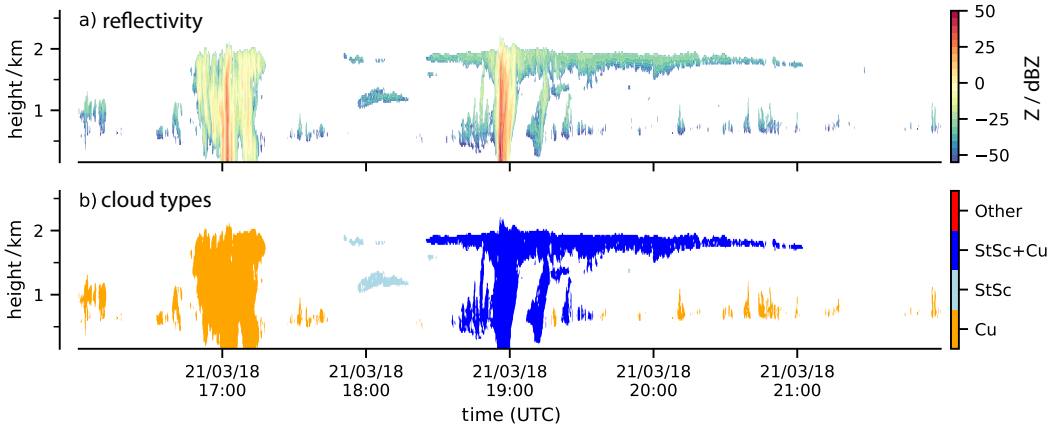

Figure 1. Example of cloud-type classification based on radar reflectivity

Similar to Lamer et al. (2015) we classify individual clouds by their cloud base heights (CBH). Stratiform layers are defined as clouds that have a frequent CBH above 1 km up to 2.5 km. If the CBH is in general below 1 km the cloud is classified as originating from the cumulus gene. An example of the radar reflectivity and the derived cloud-type classifications is shown in Fig. 1. It illustrates, that also a mixture of cumulus with an attached stratiform layer may exist. These cases are actually classified as "StSc+Cu" in the case the stratiform layer exists for at least 20 % within a cumulus cloud-entity.

Based on the single cloud entities the macro-physical properties like stratiform extent, rain flag and the mean thickness of the stratiform layer are calculated and associated with each entity.

3 Surface based characterization of cloudiness and precipitation

The four patterns identified by Stevens et al. (2020) – *Sugar*, *Gravel*, *Flowers*, *Fish*– are purely defined by their visual impression from space, predominantly the spatial distribution of cloudiness. The cloudiness is therefore the closest physical quantity to the subjective definition of these patterns. Among the physical differences that may accompany these patterns, aspects of cloudiness that go beyond the spatial arrangement of reflectivity as seen from above will be important to characterize, especially in so far as it influences the cloud radiative effect.

An overview of these patterns and the ground based observations linked to them is shown in Fig. 2. Differences in cloudiness are readily apparent, and conform to what

has been previously noted in the literature. *Sugar* is identified with a fine dusting of clouds, *Gravel* with cloud features arranged around arc-like structures. *Flowers* and *Fish* are composed of elements that are yet larger in scale and show a clearer separation between cloudy and clear-sky areas. For *Flowers* the clouds show a more isotropic distribution, while they are usually elongated – roughly West to East – in the case of *Fish*.

From these illustrations, which add to the examples shown in Stevens et al. (2020), it is natural to develop preconceptions about differences in the three dimensional structure of the boundary layer associated with the patterns. For example, *Gravel* is generally thought to be associated with precipitation due to the visible cold pool signature in the cloud field, and *Flowers* are thought to be composed of stratiform clouds with suppressed convection around them. Assessing whether such preconceptions are supported by the data, rather than manifestations of extreme and unrepresentative cases, is one of the goals of this section.

We first focus on the characteristics of the cloudiness in terms of their macro-physical and geometric properties. Thereafter we analyse the precipitation signatures of the patterns, as they might help to gain a process understanding on how these different patterns form.

3.1 Cloudiness

The cloud cover at the Barbados Cloud Observatory is shaped by the ubiquitous appearance of cumulus humilis – i.e., cumulus clouds of very limited vertical extent. Cumulus humilis are not the only cloud type measured at the site. Even in the northern hemispheric winter, when the Intertropical Convergence Zone is furthest away from Barbados and the region experiences strong subsidence, the measured cloud fraction is not solely caused by non-precipitating cumulus humilis. This is demonstrated by an analysis of the mean echo fraction profile (a combination of cloud- and rain-fraction) shown in Fig. 3. Echoes are detected extending to depths above 3 km.

Looking at the mean echo fraction profiles of *Sugar*, *Gravel*, *Flowers* and *Fish* and also the overall wintertime mean echo fraction, suggests that all but *Fish* are some breed of shallow convection, with very small echo fractions (less than 3 % at 4 km) extending much above 2.5 km. *Fish* appears distinct. Its echo fraction is larger than the seasonal

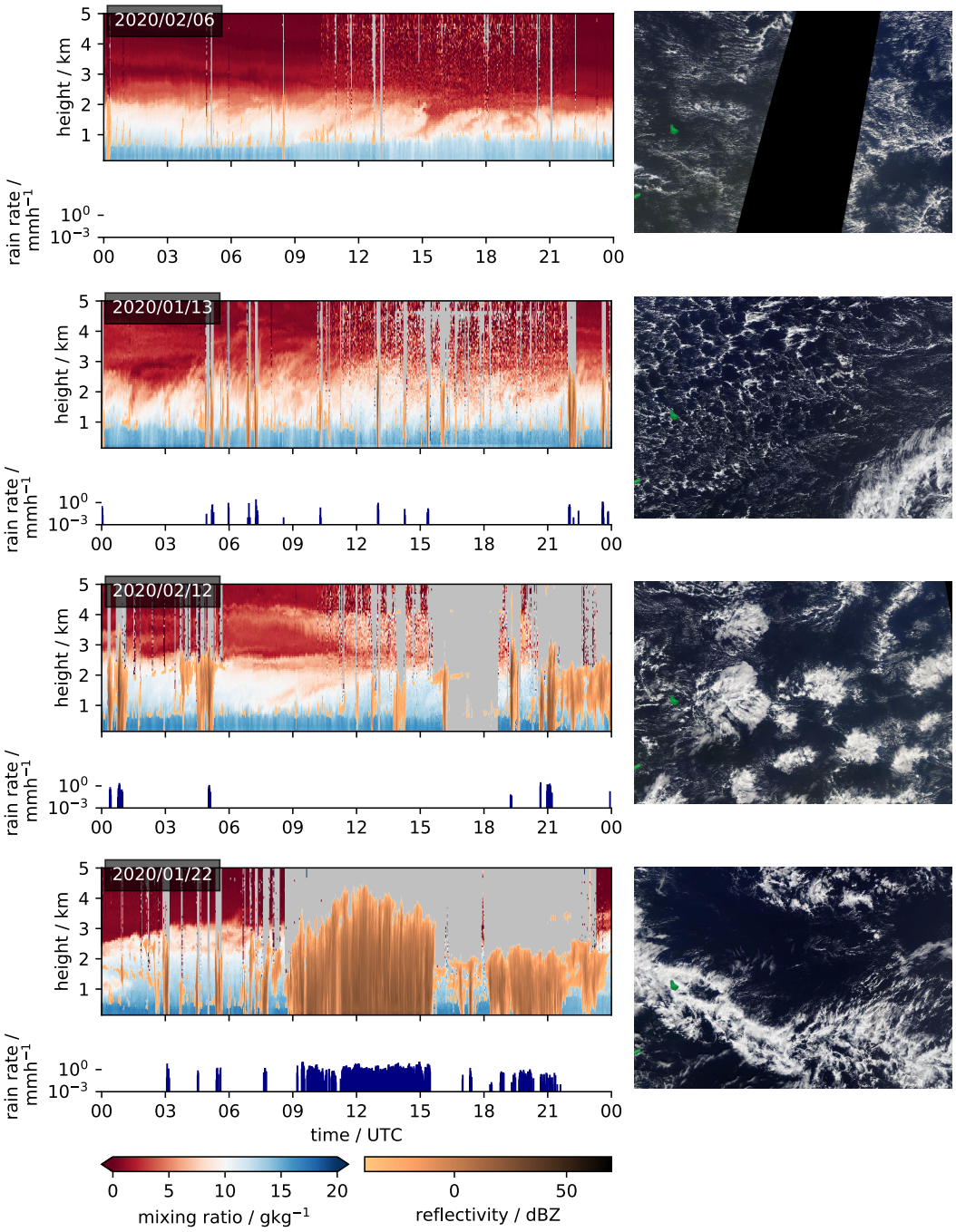

Figure 2. Time-series of each cloud pattern as identified by scientists participating in the EUREC^{4}A campaign (top to bottom: *Sugar*, *Gravel*, *Flowers*, *Fish*). Water vapor measurements from the Raman lidar overlayed by radar reflectivity shown in upper panels, while rain rates measured at 325 m are shown in the lower panels. The according MODIS images from the TERRA satellite overpass are shown on the right. Missing values are colored grey.

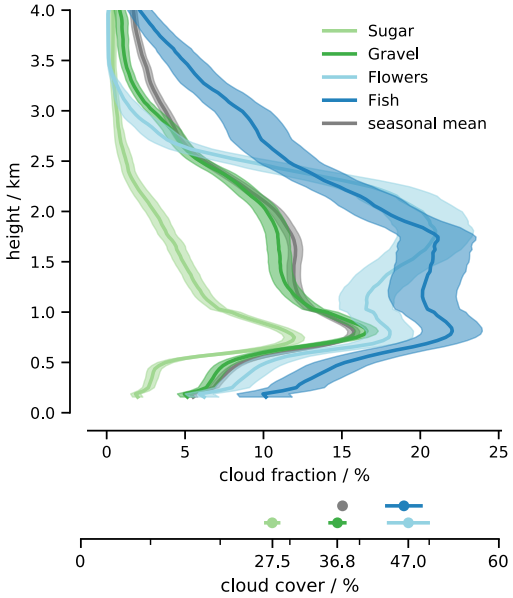

Figure 3. Echo-fraction measured at the Barbados Cloud Observatory and grouped by detected pattern indicating the combination of cloud- and rain-fraction (upper panel). The height integral, echo coverage, is shown in the bottom panel. The overall mean of the analysed winter seasons is shown in grey. Shading indicates standard error of mean.

mean, also above the moist cloud-layer usually identified with the region below the maximum echo-fraction between 2.0 km to 2.5 km.

Differences near the lifting condensation level (i.e., associated with a local maximum in the echo fraction near 750 m) are less pronounced. Here, independent of the cloud pattern, and more general independent of any observed cloud distribution, echo fractions are more similar. The lack of variability of cloud amount at the cloud-base height was emphasized by Nuijens et al. (2014). The variations that exist can largely be attributed to rain events, i.e., differences below 500 m – which are a signature of precipitation – are similar to those at 700 m. This implies that the non-raining cloud-base echo fraction differs little among the patterns and is similar to the seasonal mean. That *Flowers* would have a similar echo fraction at cloud-base after the rain correction as *Sugar* was not something we would have guessed from the satellite imagery. It shows that an abundance of clouds near cloud-base under the cloud shield compensates for an absence of shallow-cloudiness in the cloud-free part of the *Flowers* pattern.

Fig. 3 further suggests that cloudiness aloft, in the layer between 1.5 km to 2.5 km, explains a large part of the differences in the satellite imagery which gives rise to the different patterns. For instance *Flowers*, with its cloudy patches of high reflectivity paired with the sheet-like structure anticipate a strong stratiform component in the cloud fraction compared to *Sugar* and *Gravel*, as is indeed evident in the echo-fraction profiles. *Fish* has high echo-fractions throughout the cloud layer, but are less obviously dominated by a stratiform component as compared to simply more cloudiness, which often extends much more deeply through the lower troposphere. In the case of *Gravel*, a local maximum in cloudiness aloft is hardly evident and completely missing for *Sugar*. It is therefore the cloudiness aloft, that varies most with about 15 % at 1.7 km and distinguishes the cloud fraction profiles of the patterns.

Looking at the cloudiness of the patterns as a whole, we recognize, that the echo fraction of *Gravel* has the strongest similarity to the seasonal mean echo fraction, which is the average of all 6 h windows independent of any pattern. This is consistent with *Gravel* being the most common pattern detected in this study (about 19 % of all regarded time windows and 45 % of the windows with any dominant pattern). Further, it also suggests, that a large portion of the more uncertain and mixed time-windows contains cloudiness similar to the *Gravel* pattern. *Sugar*, in contrast, occurs rather more seldom. This might seem to contradict Rasp et al. (2020) who found that *Sugar* is actually more often identified than *Gravel*. However, similar to Stevens et al. (2020), who were looking for dominating patterns on a fixed domain, we look for dominating patterns within a fixed time-period. Both methods register only patterns that are persistent for a long time or cover a large area, both of which de-emphasize *Sugar*. The cloud pattern with randomly distributed clouds of little vertical extent occurs frequently, but is often not dominant and thus not picked out by our analysis.

In the following, we decompose the cloudiness further into individual cloud entities. Each of those cloud entities is then classified, as described in Sec. 2.4, into the traditional cloud genes: cumulus, stratus, or as a combination of those in case they are connected. This way, we analyze whether the patterning has an influence on the distribution, frequency and composition of cloud types. For instance, based on the above, one would immediately expect stratiform clouds to dominate for *Flowers* and be absent for *Sugar*.

The entity analysis shows the cloud base height (CBH) of cumulus, which to a first approximation is the same as the lifting condensation level of near surface air, is at about 650 m to 700 m with cloud tops about 160 m higher. Stratus are about 130 m thick on average, with an average CBH between 1600 m to 1850 m. The stratiform layers that are connected to a convective core during the time of observation have a CBH between 980 m to 1050 m and a cloud top height between 1240 m to 1370 m, which is somewhat lower than for Stratus.

Looking at single entities of the clouds detected within the classified 6 h analysis periods, we found no evidence, that the properties of the cloud elements were influenced by the pattern. We had imagined that stratiform clouds formed by *Gravel* might form more from convective outflow, and those forming in *Flowers* may form more in-situ, so that the stratiform cloud elements they incorporate would differ. To the extent such differences exist they were not detectable. What this means is that independent of the mesoscale organization, a stratiform layer, when it forms, has similar macro-physical properties across patterns e.g., for both *Flowers* and *Sugar*. The only differences are that it occurs more rarely for *Sugar* and that the size of the stratiform components ("StSc"; "StSc+Cu") increases from *Sugar* (24 km; 56 km) via *Gravel* (30 km; 84 km) to *Fish* (32 km; 181 km and *Flowers* (47 km; 151 km)). The average of the upper 5th percentile is given in brackets for the two stratiform categories as this can be assumed to better capture the characteristic length of the stratiform cloud decks by excluding very small entities and entities whose path length is much smaller than the actual characteristic length as clouds rarely drift over the observatory with the latter. The measurement time has been translated into length by assuming a mean wind speed of $10\,\mathrm{m\,s^{-1}}$ at cloud top.

As an alternative way to look for the signature of different cloud-controlling processes, Fig. 4 presents a Contoured Frequency by Altitude Diagram (CFAD) for the different patterns. It thus illustrates the frequency of occurrence of a specific reflectivity at a certain height composited on different patterns.

Some features can be identified across multiple patterns. For instance an arc-like mode, extending upward from low-reflectivities (−30 dBZ) near cloud base (0.7 km) toward higher reflectivities (15 dBZ) at about 2 km is identified with the imprint of the non-precipitating cumulus humilis (Lonitz et al., 2015). These can be found across all pat-

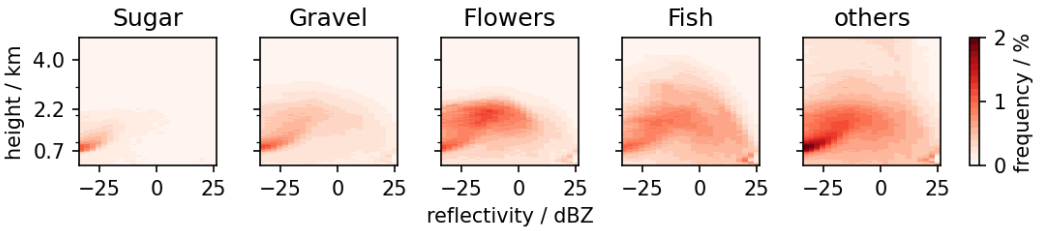

Figure 4. Contoured frequency by altitude diagram (CFAD) for the four patterns of shallow convection and less clear patterns gathered in the group *Others*. The colors indicate the frequency of occurrence of a reflectivity-height tuple within a specific pattern.

terns and contribute to a large extent to the total cloud cover of *Sugar* and *Gravel*, which is about 0.3 and 0.4, respectively (Fig. 3).

Besides the robustness of the cloudiness near cloud-base, Fig. 4 also shows that the vertical extent of clouds are more or less strongly capped at a particular height. *Sugar* echoes diminish upward with very little signal at the expected top of the moist layer, *Flowers* echoes are clearly capped at about 2.2 km. *Fish* echoes and *Others* frequently extend to 3 km and deeper with little evidence of strong capping.

The capping is not the only difference between *Flowers* and *Fish*. Despite a similar cloud cover of about 0.5, the stratiform layer differs in these cases. Whereas *Flowers* show a second distinct reflectivity maximum at about 2.2 km and near −5 dBZ, the distribution is more monomodal for *Fish*. This two-layer structure suggests that *Flowers* are only sporadically connected by higher cumulus convection whereas for *Fish*, clouds aloft appear to be deeper and as a more continuous extension of clouds near cloud base. More like a more active and deeper distribution of *Gravel*. The deeper echoes for *Fish* are also evident in a stronger precipitation feature (i.e., 25 dBZ near surface mode).

3.2 Rainfall

To assess, how important precipitation might be for different patterns, we characterize its frequency and strength in the following. From the example time-series shown in Fig. 2 and the results from the previous section, we expect a clear separation of the precipitation characteristics among the patterns: from the lack of rain during the occur-

rence of *Sugar*, to frequent showers in the case of *Gravel*, to yet stronger rain events for *Fish*.

To test this expectation, we take a look at the precipitation measurements from the BCO within the same 6-hour time windows used in the section above. First, we quantify how many analysis windows contain any rain event. With the exception of *Sugar*, in more than 50 % of the identified cases, rain is present. For *Sugar* precipitation can be detected in only 35 % of the cases.

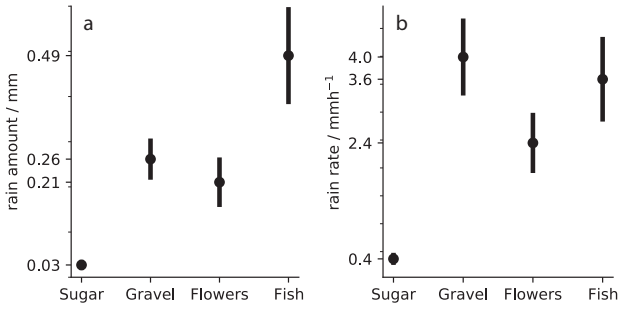

Figure 5. Rain statistics of each pattern averaged over a 6-hour period. The average rain amount (left) and the average maximum rain rate of each window (right) are shown with their standard error.

This absence of rain events in case of *Sugar* is even more evident in the quantification of the mean near-surface rainfall (Fig. 5a). Rain amounts are similar for *Flowers* and *Gravel*, consistent with the frequency of near surface echoes evident in Figs. 3 and 4, nearly twice as large for *Fish*. We also quantify rain intensity by averaging the maximum rain-rates within each analysis window for each of the patterns. Among the precipitating patterns rain intensities do not differ as substantially. In all of these cases the precipitation is intense (approach 10 cm a day), and well above the threshold (1 mm h^{-1} to 2 mm h^{-1}) that past studies have associated with the formation of cold-pools (Barnes & Garstang, 1982; Drager & van den Heever, 2017).

By applying the threshold of 1 mm h^{-1} to the maximum rain events, the number of cases with significant rainfall decreases to 12 % in case of *Sugar* and about 35 % for the other patterns. 35 % might not seem to be a lot, but it has to be kept in mind, that these patterns are of meso-scale extent and even a 6 h-period cannot capture the complete variability. This is especially the case for the *Fish* pattern, where a 6 h-period might

only capture the clear-sky part of the *Fish* and therefore the importance of precipitation can be underestimated for a single 6 h-period, especially under the assumption, that the clear-sky part depends on the dynamics in the cloudy part and cannot exist independently. *Sugar*, *Gravel* and *Flowers* all consist of several individual cloud patches, while *Fish* is often occurring as a single, large-scale network of clouds that can be separated by its equally characteristic wide-spread clear-sky areas by several hundreds of kilometers.

Our data does not contain sufficient samples to evaluate to what extent the spatio-temporal characteristics of precipitation differs among the patterns. However, by analysing the precipitation signature in all 138 6-hourly windows of *Fish*, there is evidence of a bimodal distribution of rain events, with a second mode consisting of extended periods of precipitation (like the one shown in Fig. 2) that is not evident for either the case of *Flowers* or *Gravel*.

Overall, precipitation events of significant strength occur during *Gravel*, *Flowers* and *Fish* periods and suggest to play a role in the patterning process or at least in the persistence of these patterns. There is no hint that precipitation is important for *Sugar*. To understand why these patterns are occurring in the first place, we take a look at the atmospheric environment these patterns go along with in the next section.

4 Meteorological environment

In the previous section we characterized similarities and differences in cloud- and precipitation-signatures among the four patterns. Presumable differences among patterns are not simply a random selection of different states of self-organization. To the extent the patterns are forced, this forcing might be evident in the local meteorological setting, or as a transient response to the adjustment from different upstream environments. In this section, we address the first possibility and investigate the meteorological settings, first at the surface and then within the free troposphere, for the different patterns.

4.1 Surface measurements

Near surface (5 m and 25 m above mean sea level) meteorological measurements at the BCO are composited by pattern in Fig. 6. Common to all variables shown is a distinguished value for at least one of the patterns.

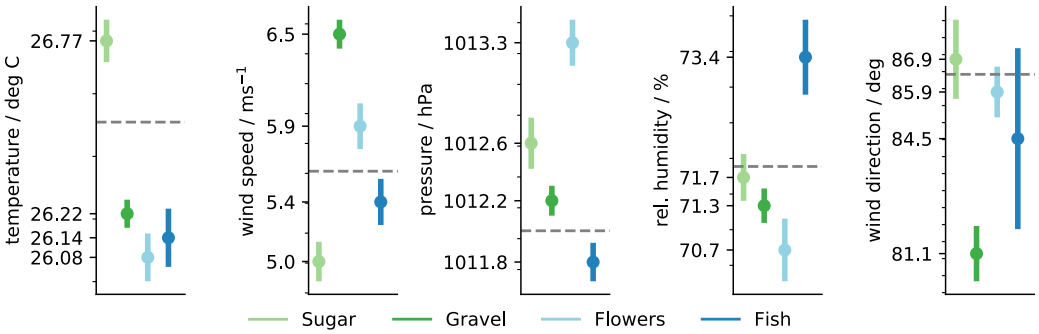

Figure 6. Surface meteorology measured at the BCO during the observation of the four patterns. The seasonal mean of the observed time-period independent of any pattern is drawn as grey line.

Sugar distinguishes itself from other patterns by virtue of its mean temperature and low wind-speed. Given that annual cycle of surface temperatures is just over 2 K this 0.6 K difference is large. While *Sugar* is associated with unseasonably warm conditions, the contrast with the other patterns is due in equal part to them being unseasonally cool, which is consistent with *Sugar* arising during periods with little northerly contribution to the mean flow. *Gravel* is distinguished by the surface winds being unseasonally strong and northerly. *Flowers* are found on the days that are coolest, when surface winds are strong, but not so strong as for *Gravel*, and when the surface pressure is unseasonally high (1013.3 hPa). In contrast *Fish* which are also associated with extensive cloud coverage (Fig. 3) are found on days with unseasonally low pressure (1011.8 hPa), high humidity and relatively low but quite variable (in terms of direction) winds, consistent with more disturbed conditions and extended periods of precipitation.

Amongst all analyzed surface observations, wind speed is the best proxy for a specific pattern. The lowest mean wind is measured during *Sugar* situations with 5 m s^{-1}. For the other patterns the mean wind speed increases by an increment of 0.5 m s^{-1} from *Fish* to *Flowers* to *Gravel*. The finding that *Flowers* and *Gravel* occur in conditions of higher winds is consistent with what was found by Bony et al. (2020), but further discriminates among all patterns rather than two groupings (e.g., *Flowers* and *Gravel* as high wind-speed and *Sugar* and *Fish* as low wind-speed patterns). We gain similar results to Bony et al. (2020) when compositing the ERA5 surface data (Fig. S1). On the one hand, this finding is indicative that the different methods to detect the meso-scale

organization are in agreement, on the other hand, it also suggests that there may be processes that are not captured by the analysis.

4.2 Vertical structure

In this section we extend the previous analysis in the vertical through a composite analysis of the Grantley Adams radiosonde data. As compared to temperature and humidity profiles derived from the Raman lidar at the BCO, the soundings have the advantage that they give meaningful profiles even in case of cloudy situations, where the lidar attenuates. The radiosondes also provide wind profiles through the depth of the troposphere (the wind lidar at the BCO mostly measured vertical wind, and then only in the lowest 1 km). The pattern mean-soundings, and their associated uncertainty estimate, are presented in Fig. 7. Composites are made of the equivalent potential temperature, potential temperature difference ($\Theta - \overline{\Theta}$, where $\overline{\Theta}$ is the mean sounding across all patterns), relative humidity and wind speed.

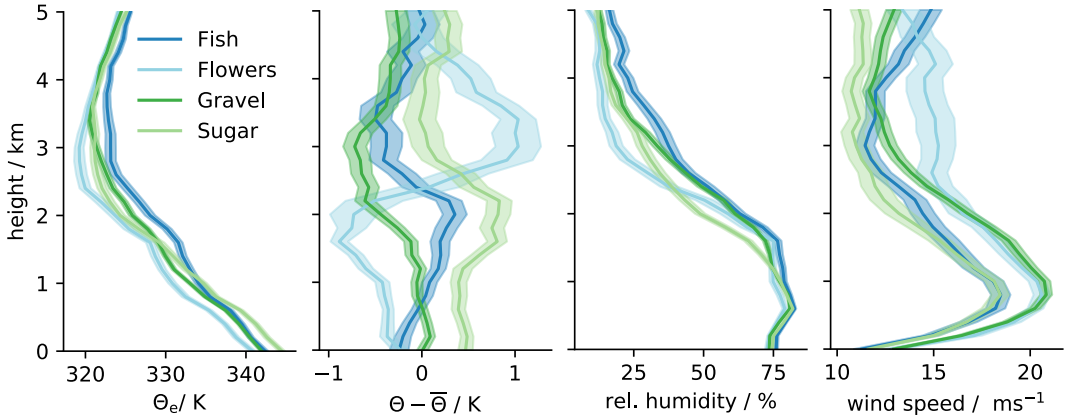

Figure 7. Average profiles of equivalent potential temperature, potential temperature difference to the overall pattern mean and relative humidity from soundings at the Grantley Adams Airport.

Surface temperature differences measured at the BCO are also evident in the soundings, and extend through the depth of the moist (lower 3 km) layer. *Flowers* distinguish themselves not only by virtue of lower surface temperatures, but also by a much stronger stratification atop the humid layer, showing a strong inversion at about 2.5 km. *Sugar* appears associated with a much shallower cloud layer, also capped by an inversion. The

apparent instability (decrease in Θ with height) for the other patterns simply indicates that they are less stable on average. The lower-tropospheric stability (LTS) is 16.2 ± 0.3K in case of *Flowers* and nearly 2 K lower for *Fish* (14.7 ± 0.2K), *Sugar* (14.4 ± 0.2K) and *Gravel* (14.1 ± 0.1K). However, in the case of *Sugar*, the value of Θ at 700 hPa (which is used to construct LTS) may miss the shallow stable layer that appears to cap the convective development of this pattern.

The relative humidity profile is strongly coupled to the convective activity and hence the echo fraction (e.g., Fig. 3) As we have shown in the last section, *Sugar* is mostly characterized by cloudiness at cloud-base height with only few clouds reaching up to 1.8 km. In agreement, the according moisture profile shows a shallower layer compared to the other patterns that more regularly reach the inversion height and distribute moisture. Likewise *Fish*, with echos reaching much more deeply through the lower troposphere is also considerably moister than the other patterns above 3 km. These humidity profiles also help explain differences in θ_e, particularly in the upper cloud layer and lower free-troposphere. For example as seen by contrasting *Fish* and *Gravel*.

Based on measurements made during RICO, Nuijens et al. (2009) analyzed differences in θ_e similar to those shown in Fig. 7. Consistent with their findings these profiles seem to co-vary consistently with surface wind speeds. Stronger surface winds for *Gravel* and *Flowers* are mostly confined to the moist layer for *Gravel*, but extend through the lower troposphere for *Flowers*. These winds are one component of what is often thought of as an externally imposed large-scale forcing, to which the boundary layer thermodynamic profiles relatively quickly equilibrate. Other aspects of this forcing, like the lower tropospheric stability and large-scale subsidence are examined in more detail next.

4.3 Large-scale forcing

We first examine how the large-scale subsidence (ω_{500}) varies as a function of pattern. To better judge on which scale the forcing acts, we retrieve ERA5 data in a $20° \times 20°$ domain centered around each classification of the neural network. Those domains are afterwards averaged to one composite that shows the strength of subsidence at the center of each pattern, but also in its surrounding.

Fig. 8 reveals, that all patterns occur during times of subsidence and that this subsidence is in most cases also similar to the typical subsidence rate of $0.05\,\mathrm{hPa\,s^{-1}}$ in the

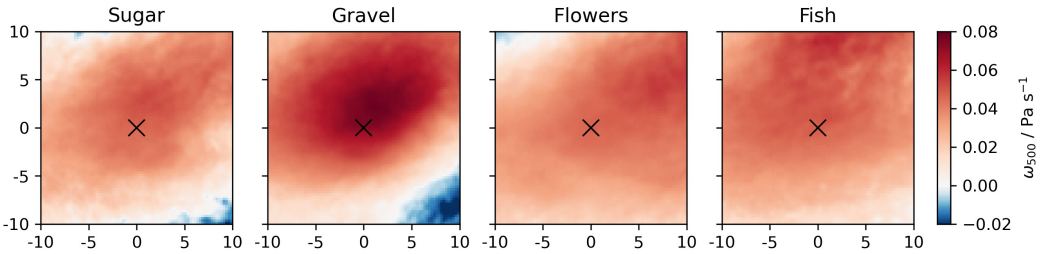

Figure 8. Distribution of subsidence strength ω_{500} relative to identified pattern centers composited by 20x20 degree domains around each identified pattern. Pattern centers are marked with a cross.

Atlantic trade-wind regime (Holland & Rasmusson, 1973). However, it also shows that some variability in the large-scale forcing exists and stronger subsidence is, contrary to expectation, not occurring during *Sugar* and *Flowers* cases, but rather during *Gravel* cases (Tab. 2).

Table 2. Large-scale forcing averaged by pattern from fixed-location sounding data (snd) and ERA5 data from pattern center

Pattern	$\mathrm{LTS_{snd}}$	$\mathrm{LTS_{ERA5}}$	$\omega_{500,\mathrm{ERA5}}$	freq. of convergence
Sugar	14.4 K	14.8 K	0.046 Pa s^{-1}	28%
Gravel	14.1 K	14.4 K	0.072 Pa s^{-1}	38%
Flowers	16.2 K	16.6 K	0.046 Pa s^{-1}	34%
Fish	14.7 K	16.0 K	0.048 Pa s^{-1}	59%

In the subtropics, particularly in association with stratocumulus, subsidence covaries positively with LTS. On shorter time scales and deeper in the tropics, other factors may play a role. In particular the temperatures above the cloud layer are more tightly coupled to moisture, so as to homogenize the density temperature on isobaric surfaces. This partly explains the stronger temperature inversion for *Flowers*. It also means that boundary layer variability may play a more important role in determining the LTS, consistent with near-surface temperature differences as illustrated in Fig. 6. These in turn may be influenced by the upstream conditions that the patterns sample, something we explore with the aid of back-trajectories in the next section.

5 Are the four patterns indicative of specific air masses?

The four patterns occur preferentially in atmospheric conditions intrinsic to the maritime trade-wind regions.

Rasp et al. (2020) showed that globally, the four patterns predominate in the dry tropics, regions often associated with the trade winds. The analysis in the previous section identified subtle differences in the environments in which the four patterns form. This raises the question as to the origin of these environmental differences, i.e., to what extent they arise from subtle variations within the trades, or what one might alternatively think of as disturbances to or departures from canonical trade-wind conditions. We explore this question by analysing the seasonal cycle of the four patterns within our North Atlantic study region as well as the air-mass histories of the different patterns by compositing reanalysis data along back-trajectories constructed from that same data.

5.1 Seasonality

Seasonality is investigated using 10 years of MODIS AQUA daytime overpasses (2010-2020). The neural network classification is applied over the Tropical and North Atlantic, the results of which (Fig. 9) are presented in the form of spatial histograms of occurrence for each pattern for three seasons.

Considering just the region of the downstream trades, taken to be the tropical North Atlantic west of 45°W, all four patterns prevail. With the exception of *Sugar*, the absence of the four patterns in this region in other seasons supports their association with the winter trades. *Fish* and *Gravel* seem only to occur in this region in conditions (DJF) when the trades are well developed. *Flowers* are also identified in the upstream trades, increasingly so in boreal spring and early summer (AMJ). *Sugar* shows very little seasonality. Rather, and consistent with the analysis by Rasp et al. (2020), it appears associated with suppressed conditions bordering the ITCZ whose seasonal migration it follows. Based on this we hesitate to call *Sugar* a trade-wind cloud pattern.

Flowers are even more common in the 'upper' trades (east of 45°W), even more so in the April-June period, (e.g., Fig. 9). Such a distribution is consistent with an affinity for conditions that favor stratocumulus. This distribution is in agreement with the analysis in the previous section, which showed that *Flowers* favor conditions of higher

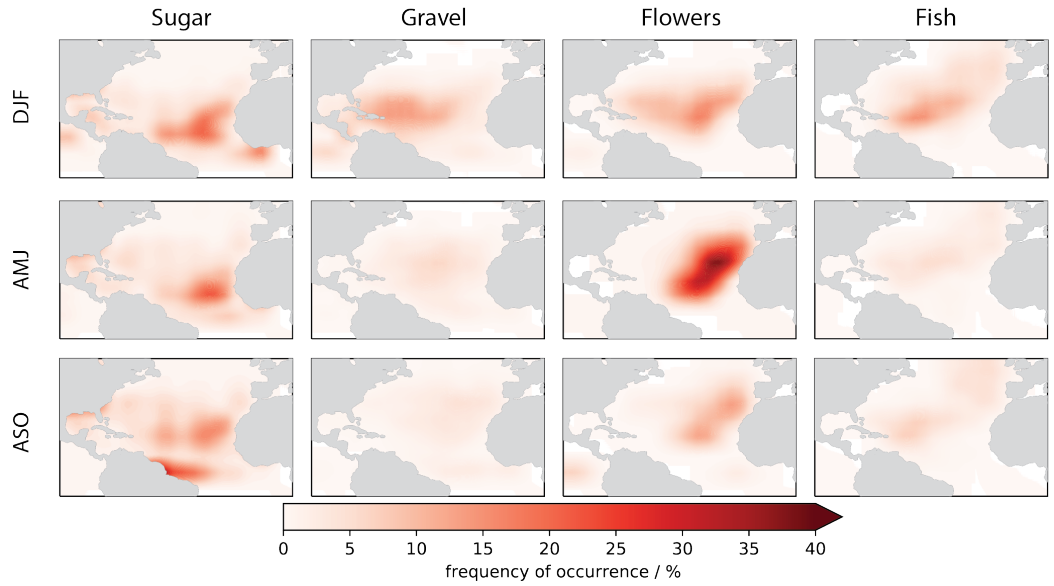

Figure 9. Seasonal distribution of patterns in the North Atlantic in the dry- (DJF), transitional- (AMJ) and wet- (ASO) season (top to bottom) detected in infrared imagery (AQUA MODIS 2010-2020).

lower tropospheric stability, and lower surface temperatures, as compared to the other patterns. This supports the idea that *Flowers* are the downstream manifestation of the familiar, but much smaller, closed cellular stratocumulus (Stevens et al., 2020); alternatively, it may be indicative of a failing of the neural network to distinguish between *Flowers* and closed-cells.

The strong association of *Flowers*, *Fish* and *Gravel* with the down-stream trades in winter (when they are most developed), suggests that the origin of their differing environmental conditions may have less to do with the intrusion of different regimes, and more to do with the nuanced evolution of the winter trades.

5.2 Lagrangian evolution of air masses by meso-scale organization

Here we use the back-trajectories, initialized at the center of the classifications following the boundary layer winds at 925 hPa for 84 h, to investigate possible reasons for the environmental differences associated with each pattern.

Fig. 10 shows that the back-trajectories are consistent with the steadiness that characterizes the winter trades, with the trajectories aligning well along the general flow of

the trades as they come to their point of initialization. They do however differentiate themselves as one follows their history back in time. Most notably *Fish* which originates far to the west of the other trajectories. A more tropical influence on *Sugar*, is also consistent with its back-trajectories which start furthest south.

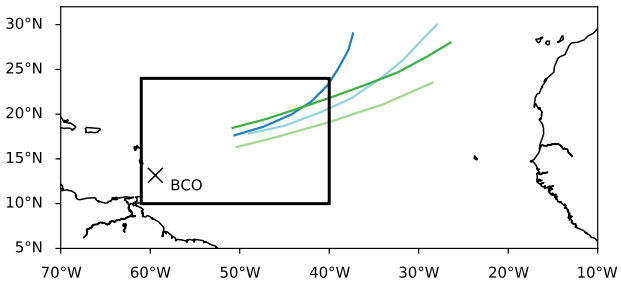

Figure 10. Mean back-trajectories for the different patterns initialized at the center of individual classifications within the indicated black box at 925 hPa and calculated for 84 h.

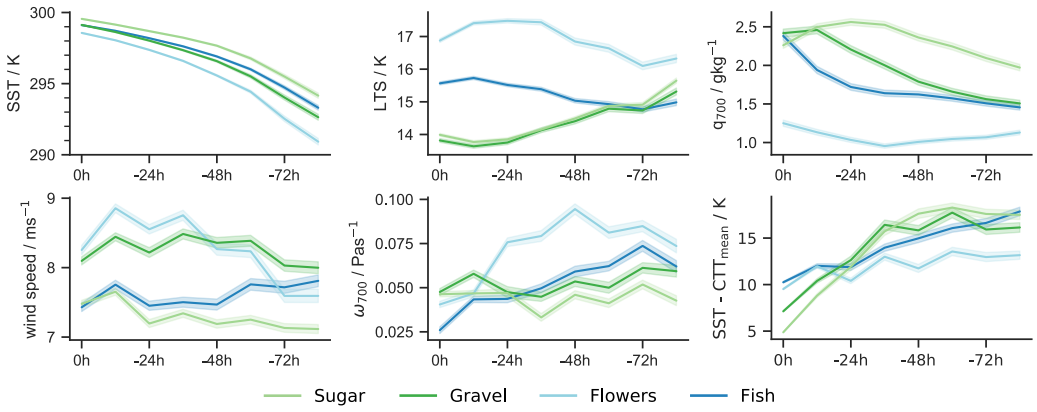

Figure 11. Environmental conditions along the back-trajectory. All values are ERA5 reanalysis properties, except the cloud top height estimate where the cloud top temperature (CTT) is sourced from MODIS AQUA observations. Shading indicates standard error.

Compositing the large-scale conditions, as given by the ERA5 reanalysis products, along the trajectories yields further insight into factors influencing the environmental conditions associated with each of the four patterns. This analysis is presented in Fig. 11.

This analysis is largely consistent with what was shown in the previous section, and furthermore shows that many of the environmental differences previously documented are apparent well in advance (and upstream) of where the pattern was eventually iden-

tified. *Sugar* has warmer sea-surface temperatures, weaker winds and a relatively moist free-troposphere along its entire back-trajectory, consistent with a more tropical influence. *Flowers* evolve over cold ocean temperatures throughout the trajectory paired with persistently high LTS (despite rising SSTs), a dry free troposphere and stronger low-level winds. And differences in LTS among the patterns are robust and in place already 48 h earlier.

The time-evolution of different fields is also indicative of dynamic influences. For instance, for *Flowers* an acceleration of the low-level winds between −24 h to −84 h may be driving the strong subsidence at 700 hPa, which in turn would support the anomalously dry free-troposphere and high LTS. This pattern preceding process may drive the differences between *Flowers* from *Gravel* with the slight slackening of the winds and the decrease of the subsidence nearer the time and place where the pattern is identified, playing less of a role. In contrast, for *Fish* a strong temporal evolution within the last 24 h, as manifested by a pronounced moistening of the lower troposphere, might be indicative of a dynamic disturbance. *Sugar* seems less representative of a sudden stilling in the winds in association with *local* suppression, if anything recovering from more suppressed conditions and weaker winds upstream.

The time-evolution of cloud top height, estimated as the difference between the ERA5 sea surface temperature and the mean cloud top temperature sourced from MODIS within 100 km around the trajectory sampling point, can further be an indication of different lifetimes of the patterns. *Sugar* and *Gravel* seem to set up only shortly before the detection (-36h) when the cloud top height dropped quickly, which would be indicative of a shorter lifetime. In contrast, *Flowers* and *Fish* might have persisted longer at the time of detection because the cloud top height evolves only little. The diurnality that is pronounced in a number of fields (wind speed, ω_{700}, SST-CTT) is explored in more depth by Vial et al. (submitted).

In the following, we explore the idea that *Fish* is more disturbance driven with the help of a case study.

5.3 Extra-tropical disturbances

Although we focus on the northern hemispheric winter season where the trades are well formed, disturbances to the trade-wind mean flow are well documented (Bunker et

al., 1949; Riehl, 1945). The earlier literature identifies two types of disturbances, one associated with anomalously deep easterlies (which might be associated with active deep convection), the other associated with extra-tropical intrusions in the form of trailing cold-fronts from extra-tropical cyclones.

The older literature conceptualized the later (extra-tropical intrusions) as tropical incursions of the 'polar front'. Especially in the boreal winter, when the Intertropical Convergence Zone is further south and the Azores high is less well established, frontal disturbances can extend equator-ward. By the time they reach the subtropics, their temperature signature is muted and they become most pronounced in the form of a shear line that separates the light easterlies from the stronger north-easterlies and remains (Riehl, 1945).

Such a frontal passage can be seen in the surface analysis charts e.g. in association with a deepening cyclone over the mid-Atlantic (near 45°N and 45°W) on 25th December 2018. Through the course of six days the cold front, initially supported by the outflow of cold-continental air (a cold air outbreak) from the east-coast of North-America, occludes upon reaching the tropics as far south as Barbados (see Fig. 12).

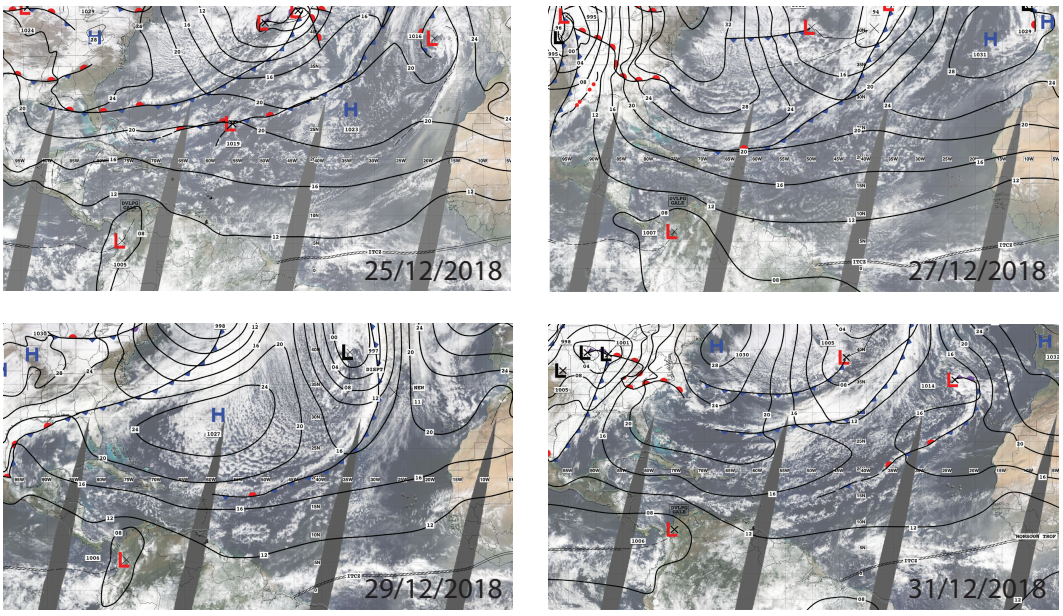

Figure 12. Cold air outbreak between 25th of December 2018 and 31th December 2018. Surface analysis charts from the National Hurricane Center are adapted and overlaid on Terra MODIS images

By comparing the surface analysis chart with the satellite image, we recognise that the front is visible as a band of convection that we would classify as *Fish*. In the former cold sector, just north of the front, one can also notice on the 29th December cloud structures north of the front similar to *Flowers* (more pronounced to the west) or perhaps *Gravel*.

We repeat our composite analyses done to create Fig. 8 with surface convergence to test, whether the frontal character is typical for *Fish* and whether other patterns can be related to the fronts as well. We find a strong signal of convergence stronger than $-1 \times 10^{-6}\,\mathrm{s}^{-1}$ (following Weller et al. (2017)) connected with *Fish* about 60 % of the identified cases (Fig. 13). A clear signature for the other patterns is less pronounced, although the absence of convergence for *Sugar* is consistent with it being more locally suppressed. For *Fish*, the pattern of convergence extents zonally in a way that supports the hypothesis of *Fish* arising in association with disturbances associated with trailing cold-fronts or shear-lines from extra-tropical intrusions.

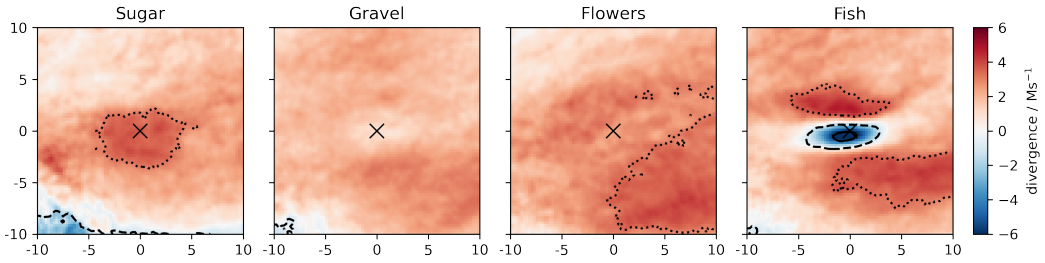

Figure 13. Distribution of divergence at 950 hPa relative to identified pattern centers composited by 20x20 degree domains around each identified pattern. Counters indicate frequency of events with convergence larger $-1 \times 10^{-6}\,\mathrm{s}^{-1}$ (30%: dotted, 45%: dashed, 60%: solid). Pattern centers are marked with a cross.

6 Discussion and conclusion

Cloud- and environmental properties associated with four patterns of meso-scale organization in the lower trades (50°W to 60°W) of the North Atlantic are examined. The four patterns follow the *Sugar*, *Gravel*, *Fish*, *Flowers* taxonomy of Stevens et al. (2020) and are identified using a neural-network applied to high-resolution infra-red imagery from the GOES16 satellite.

We conditioned surface observations, back-trajectories, and reanalysis data on the identification of different patterns to answer three questions: One, do the four patterns show physical differences in the cloud macro-physical properties as seen by surface based remote sensing? Two, can differences in the large-scale environment associated with different patterns be discerned? And, three can we identify the origins of discernible environmental differences among the patterns.

Fig. 14 summarizes these results and illustrates, that the four patterns differ in more than just their satellite presentation. Cloud coverage and its vertical distribution differ and differences in the environment of different patterns are discernible. The thermodynamic profiles in Fig. 14 show inter-pattern differences, but also intra-pattern differences as measured by radiosondes at points whose position relative to other features within a pattern is schematized.

Many preconceptions from earlier studies, either inferred from snapshots (Stevens et al., 2020) or from compositing reanalysis data on values of a cloud-clustering index that correlate with different patterns (Bony et al., 2020), are supported by our analysis. As an example, *Flowers*, and to some extent *Fish*, have a stratiform component detectable from surface-based remote sensing. In the latter this is less distinctly a capping stratiform, or stratocumulus layer, as it is associated with more cloudiness throughout the cloud layer. Compared to the mean conditions, or the other patterns, LTS is higher (0.5 K to 1.0 K) for *Fish* and (2 K) for *Flowers*.

Non-precipitating cloud coverage at the the lifting condensation level, as emphasized by Nuijens et al. (2014) for the entirety of trade-wind cloudiness, also holds across the four patterns. This came as a surprise given that *Flowers* and *Fish* are characterized in part by their cloud free areas. Differences in cloud-base echo fraction largely reflect differences in precipitation, suggesting that to the extent environmental conditions demand an increase in the mass flux out of the subcloud layer, for instance as shown by George et al. (2020), this is largely associated with the development of deeper clouds and precipitation.

Similar to what was found by (Bony et al., 2020), near surface winds identify *Flowers* and *Gravel* with strong near-surface winds, and *Fish* and *Sugar* with light winds. Our analysis, further discriminates within these two groups, with *Sugar*, *Fish*, *Flowers* and *Gravel* each being separated by a roughly $0.5\,\mathrm{m\,s^{-1}}$ increase in surface wind speeds.

Precipitation increases with near surface winds, as previously noted for measurements during RICO (Nuijens et al., 2009), with *Fish* being an outlier whose large rain rates are associated with extra-tropical disturbances and anomalous low-level convergence.

Seasonal variations and back-trajectories provide further insight into the origin of differences in the environments of the different patterns. The view of trade-wind clouds as cumulus humilis, and hence non-precipitating with little vertical extent, as popularized by studies based on data from BOMEX (Siebesma & Cuijpers, 1995) and most closely associated with *Sugar* suggests that these are rather uncharacteristic of the trades. *Sugar* is found to favor more suppressed conditions, uncharacteristically (for the trades) weak winds, and proximity to deeper convection in the ITCZ.

As a historical note, the third author recalls that when the large-eddy simulation community began focusing on shallow trade-wind convection through simulations of conditions derived from BOMEX data (Siebesma et al., 2003), Bruce Albrecht admonished us that less suppressed and more stratiform capped conditions – as for instance seen and simulated in association with the Atlantic Trade-Wind Experiment (Stevens et al., 2001, ATEX) and which we might today call *Flowers*– were more characteristic of the Trades. We find confirmation for his point of view, twenty years later, in our data. Given the association of *Fish* with shear lines from remnant extra-tropical cold fronts intruding deep into the sub-tropics, only *Gravel* is left to add to *Flowers* as an archetypical form of trade-wind convection. *Fish* and *Sugar* are intruders.

Gravel and *Flowers* differ substantially in their cloud amounts (as seen here) and their cloud radiative effects, as shown by Bony et al. (2020). Our analysis suggests that this difference can be attributed to slightly weaker winds, and a substantially warmer and drier free-troposphere in the case of *Flowers*. This supports the development of a stronger capping inversion, and stronger boundary layer cooling. Based on back-trajectories we hypothesize that these conditions arise from an acceleration of the trades and stronger subsidence in the upstream flow along *Flowers* back-trajectories. This hypothesis lends itself well to tests with LES, and may even be evident at the somewhat coarser resolution now being simulated by a new generation of global storm-resolving models.

Independent of the formation mechanism, understanding of the conditions favoring one or the other pattern may help anticipate to what extent climate change, by virtue of changes in wind-speeds, or the frequency of extra-tropical disturbances, or changes

in the opacity and stability of the free troposphere, will color the frequency of different patterns, and thus cloud-radiative effects in the lower trades.

Open Research

Primary data and scripts used in the analysis and other supplementary information that may be useful in reproducing the authors' work can be obtained from `10.5281/zenodo.4432542`. The ERA5 datasets used in this study (Hersbach, H. et al., 2018a, 2018b) have been provided by the Climate Data Store. GOES-16 Advanced Baseline Imager Level 1b Radiances are available at `https://doi.org/10.7289/V5BV7DSR`. MODIS imagery originates from the NASA Worldview application (`https://worldview.earthdata.nasa.gov`), part of the NASA Earth Observing System Data and Information System (EOSDIS).

Acknowledgments

We thank the members of the Tropical Cloud Observation group for maintaining the Barbados Cloud Observatory and fruitful discussions. We would also like to thank Jiawei Bao for helpful comments on an earlier version of this manuscript.

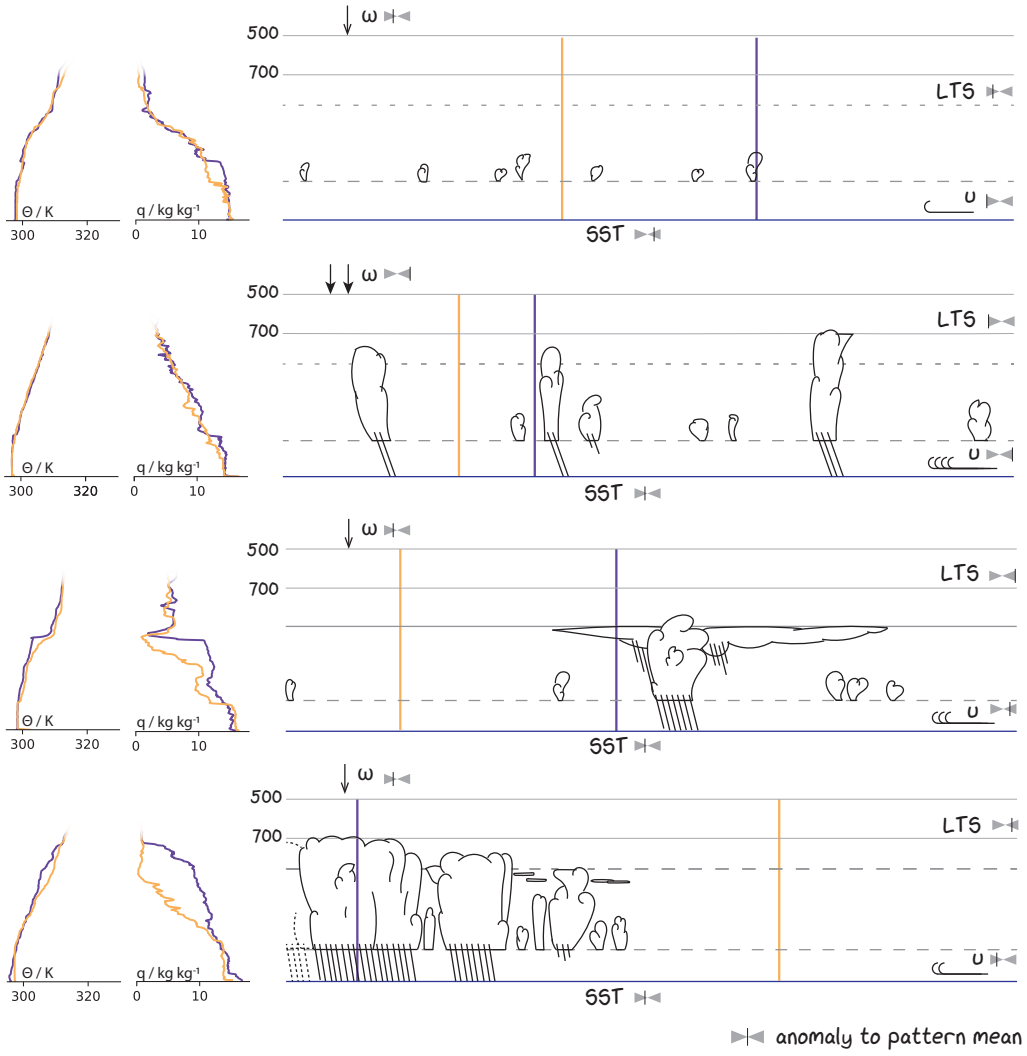

Figure 14. Illustration of the cloud field during the four patterns of meso-scale organization and the associated large-scale forcing (right) including the thermodynamic profiles (left). The anomaly in forcing to the pattern mean is indicated by grey sliders. Vertical lines indicate the contrasting positions of the thermodynamic profiles, purple being in the moist part and orange in the dry area. Thermodynamic profiles are based on soundings during the EUREC^{4}A field campaign (Stephan et al., 2020)

.

References

Agee, E. M. (1987, January). Mesoscale cellular convection over the oceans. *Dynamics of Atmospheres and Oceans*, *10*(4), 317–341. doi: 10.1016/0377-0265(87)90023-6

Atkinson B. W., & Wu Zhang J. (1996, November). Mesoscale shallow convection in the atmosphere. *Reviews of Geophysics*, *34*(4), 403–431. doi: 10.1029/96RG02623

Barnes, G. M., & Garstang, M. (1982, February). Subcloud Layer Energetics of Precipitating Convection. *Monthly Weather Review*, *110*(2), 102–117. doi: 10.1175/1520-0493(1982)110⟨0102:SLEOPC⟩2.0.CO;2

Bony, S., & Dufresne, J.-L. (2005). Marine boundary layer clouds at the heart of tropical cloud feedback uncertainties in climate models. *Geophysical Research Letters*, *32*(20), n/a–n/a. doi: 10.1029/2005GL023851

Bony, S., Schulz, H., Vial, J., & Stevens, B. (2020). Sugar, Gravel, Fish, and Flowers: Dependence of Mesoscale Patterns of Trade-Wind Clouds on Environmental Conditions. *Geophysical Research Letters*, *47*(7), e2019GL085988. doi: 10.1029/2019GL085988

Bunker, A. F., Haurwitz, B., Bernhard, Malkus, Joanne Starr, & Stommel, Henry M. (1949). Vertical distribution of temperature and humidity over the Caribbean Sea. *PAPERS IN PHYSICAL OCEANOGRAPHY AND METEOROLOGY*, *11*(1), 82.

Drager, A. J., & van den Heever, S. C. (2017). Characterizing convective cold pools. *Journal of Advances in Modeling Earth Systems*, *9*(2), 1091–1115. doi: 10.1002/2016MS000788

Eastman, R., & Wood, R. (2016, January). Factors Controlling Low-Cloud Evolution over the Eastern Subtropical Oceans: A Lagrangian Perspective Using the A-Train Satellites. *Journal of the Atmospheric Sciences*, *73*(1), 331–351. doi: 10.1175/JAS-D-15-0193.1

George, G., Stevens, B., Bony, S., Klingebiel, M., & Vogel, R. (2020). Observed impact of meso-scale vertical motion on cloudiness. *J. Atmos. Sci.*, 1–30.

Hersbach, H., Bell, B., Berrisford, P., Hirahara, S., Horányi, A., Muñoz-Sabater, J., ... Thépaut, J.-N. (2020). The ERA5 global reanalysis. *Quarterly Journal of the Royal Meteorological Society*, *146*(730), 1999–2049. doi: 10.1002/qj.3803

Hersbach, H., Bell, B., Berrisford, P., Biavati, G., Horányi, A., Muñoz Sabater, J., ... Thépaut, J-N. (2018a). *ERA5 hourly data on pressure levels from 1979 to present.* Copernicus Climate Change Service (C3S) Climate Data Store (CDS). doi: 10.24381/cds.bd0915c6

Hersbach, H., Bell, B., Berrisford, P., Biavati, G., Horányi, A., Muñoz Sabater, J., ... Thépaut, J-N. (2018b). *ERA5 hourly data on single levels from 1979 to present.* Copernicus Climate Change Service (C3S) Climate Data Store (CDS). doi: 10.24381/cds.adbb2d47

Holland, J. Z., & Rasmusson, E. M. (1973, January). Measurements of the Atmospheric Mass, Energy, and Momentum Budgets Over a 500-Kilometer Square of Tropical Ocean. *Monthly Weather Review*, *101*(1), 44–55. doi: 10.1175/1520-0493(1973)101⟨0044:MOTAME⟩2.3.CO;2

Klingebiel, M., Ghate, V. P., Naumann, A. K., Ditas, F., Pöhlker, M. L., Pöhlker, C., ... Stevens, B. (2019, February). Remote Sensing of Sea Salt Aerosol below Trade Wind Clouds. *Journal of the Atmospheric Sciences*, *76*(5), 1189–1202. doi: 10.1175/JAS-D-18-0139.1

Lamer, K., Kollias, P., & Nuijens, L. (2015, June). Observations of the variability of shallow trade wind cumulus cloudiness and mass flux. *Journal of Geophysical Research: Atmospheres*, *120*(12), 2014JD022950. doi: 10.1002/2014JD022950

Lonitz, K., Stevens, B., Nuijens, L., Sant, V., Hirsch, L., & Seifert, A. (2015, December). The Signature of Aerosols and Meteorology in Long-Term Cloud Radar Observations of Trade Wind Cumuli. *Journal of the Atmospheric Sciences*, *72*(12), 4643–4659. doi: 10.1175/JAS-D-14-0348.1

Medeiros, B., & Nuijens, L. (2016, May). Clouds at Barbados are representative of clouds across the trade wind regions in observations and climate models. *Proceedings of the National Academy of Sciences*, *113*(22), E3062-E3070. doi: 10.1073/pnas.1521494113

Nuijens, L., Serikov, I., Hirsch, L., Lonitz, K., & Stevens, B. (2014, October). The distribution and variability of low-level cloud in the North Atlantic trades. *Quarterly Journal of the Royal Meteorological Society*, *140*(684), 2364–2374. doi: 10.1002/qj.2307

Nuijens, L., Stevens, B., & Siebesma, A. P. (2009, July). The Environment of Precipitating Shallow Cumulus Convection. *Journal of the Atmospheric Sciences*,

66(7), 1962–1979. doi: 10.1175/2008JAS2841.1

Nuijens, Louise, & Jakob, Christian. (2020). Cloudy Perspectives. In A. P. Siebesma, B. Stevens, C. Jakob, & S. Bony (Eds.), *Clouds and Climate: Climate Science's Greatest Challenge* (pp. 1–32). Cambridge: Cambridge University Press. doi: 10.1017/9781107447738.002

Rasp, S., Schulz, H., Bony, S., & Stevens, B. (2020). Combining crowd-sourcing and deep learning to explore the meso-scale organization of shallow convection. *Bulletin of the American Meteorological Society*, 1–39. doi: 10.1175/BAMS-D-19-0324.1

Rauber, R. M., Ochs, H. T., Di Girolamo, L., Göke, S., Snodgrass, E., Stevens, B., ... Twohy, C. H. (2007, December). Rain in Shallow Cumulus Over the Ocean: The RICO Campaign. *Bulletin of the American Meteorological Society*, *88*(12), 1912–1928. doi: 10.1175/BAMS-88-12-1912

Riehl, H. (1945). *Waves in the easterlies and the polar front in the tropics: A report on research conducted at the Institute of Tropical Meteorology of the University of Chicago at the University of Puerto Rico, Rio Piedras, P.R.* Chicago, Ill.: University of Chicago Press.

Seifert, A., & Heus, T. (2013, June). Large-eddy simulation of organized precipitating trade wind cumulus clouds. *Atmos. Chem. Phys.*, *13*(11), 5631–5645. doi: 10.5194/acp-13-5631-2013

Seifert, A., Heus, T., Pincus, R., & Stevens, B. (2015, December). Large-eddy simulation of the transient and near-equilibrium behavior of precipitating shallow convection. *Journal of Advances in Modeling Earth Systems*, *7*(4), 1918–1937. doi: 10.1002/2015MS000489

Siebesma, A. P., Bretherton, C. S., Brown, A., Chlond, A., Cuxart, J., Duynkerke, P. G., ... Stevens, D. E. (2003). A Large Eddy Simulation Intercomparison Study of Shallow Cumulus Convection. *J. Atmos. Sci.*, *60*, 19.

Siebesma, A. P., & Cuijpers, J. W. M. (1995, March). Evaluation of Parametric Assumptions for Shallow Cumulus Convection. *Journal of the Atmospheric Sciences*, *52*(6), 650–666. doi: 10.1175/1520-0469(1995)052⟨0650:EOPAFS⟩2.0.CO;2

Stephan, C., Schnitt, S., Bellenger, H., Schulz, H., Szoeke, S. P. D., Acquistapace, C., ... Stevens, B. (2020). *Radiosonde measurements from the EUREC4A field*

765 *campaign.* AERIS. doi: 10.25326/62

766 Stevens, B., Ackerman, A. S., Albrecht, B. A., Brown, A. R., Chlond, A., Cuxart,
767 J., ... Stevens, D. E. (2001, July). Simulations of Trade Wind Cumuli under
768 a Strong Inversion. *Journal of the Atmospheric Sciences*, *58*(14), 1870–1891.
769 doi: 10.1175/1520-0469(2001)058⟨1870:SOTWCU⟩2.0.CO;2

770 Stevens, B., Bony, S., Brogniez, H., Hentgen, L., Hohenegger, C., Kiemle, C., ...
771 Zuidema, P. (2020). Sugar, gravel, fish and flowers: Mesoscale cloud patterns
772 in the trade winds. *Quarterly Journal of the Royal Meteorological Society*,
773 *146*(726), 141–152. doi: 10.1002/qj.3662

774 Stevens, B., Farrell, D., Hirsch, L., Jansen, F., Nuijens, L., Serikov, I., ... Pros-
775 pero, J. M. (2016, May). The Barbados Cloud Observatory: Anchor-
776 ing Investigations of Clouds and Circulation on the Edge of the ITCZ.
777 *Bulletin of the American Meteorological Society*, *97*(5), 787–801. doi:
778 10.1175/BAMS-D-14-00247.1

779 Vial, J., Vogel, R., & Schulz, H. (submitted). The role of mesoscale cloud organi-
780 zation in the daily cycle of trade-wind cumuli. *Quarterly Journal of the Royal*
781 *Meteorological Society*.

782 Weller, E., Shelton, K., Reeder, M. J., & Jakob, C. (2017, May). Precipitation As-
783 sociated with Convergence Lines. *Journal of Climate*, *30*(9), 3169–3183. doi:
784 10.1175/JCLI-D-16-0535.1

785 WMO. (2017). *International cloud atlas*. World Meteorological Organization.

786 Young, G. S., Kristovich, D. A. R., Hjelmfelt, M. R., & Foster, R. C. (2002,
787 July). ROLLS, STREETS, WAVES, AND MORE: A Review of Quasi-
788 Two-Dimensional Structures in the Atmospheric Boundary Layer. *Bul-*
789 *letin of the American Meteorological Society*, *83*(7), 997–1002. doi:
790 10.1175/1520-0477(2002)083⟨0997:RSWAMA⟩2.3.CO;2

791 Zuidema, P., Li, Z., Hill, R. J., Bariteau, L., Rilling, B., Fairall, C., ... Hare, J.
792 (2012, January). On Trade Wind Cumulus Cold Pools. *Journal of the Atmo-*
793 *spheric Sciences*, *69*(1), 258–280. doi: 10.1175/JAS-D-11-0143.1